# Imaging and Quantifying the Formation of Single Nanobubbles at Single Platinum Nanoparticles during the Hydrogen Evolution Reaction

Jean-François Lemineur, Paolo Ciocci, Jean-Marc Noël, Hongxin Ge, Catherine Combellas, Frédéric Kanoufi

# Imaging and Quantifying the Formation of Single Nanobubbles at Single Platinum Nanoparticles During the Hydrogen Evolution Reaction.

*Jean-François Lemineur, Paolo Ciocci, Jean-Marc Noël, Hongxin Ge, Catherine Combellas, and Frédéric Kanoufi**

Université de Paris, ITODYS, CNRS, F-75006 Paris, France.

ABSTRACT. While numerous efforts are produced towards the design of sustainable and efficient nano-catalysts of hydrogen evolution reaction (HER), there is a need for the *operando* observation and quantification of gas nanobubbles (NBs) formation involved in this electrochemical reaction. It is achieved herein through interference reflection microscopy (IRM) coupled to electrochemistry and optical modelling. Besides analyzing the geometry and growth rate of individual NBs at single nanocatalysts, the toolbox offered by super-localization and quantitative label-free optical microscopy allows analyzing the geometry (contact angle and footprint with surface) of individual NBs and their growth rate. It turns out that after few seconds, NBs are steadily growing while they are fully covering the Pt NPs that allowed their nucleation and their pinning on the electrode surface. It then raises relevant questions related to gas evolution catalysts as for example: does the evaluation of NB growth at single nano-catalyst really reflect its electrochemical activity?

KEYWORDS. single-entity electrochemistry, optics, modeling, same location microscopy, nanobubbles, platinum nanocatalysts.

## INTRODUCTION

Gas nanobubbles (NBs) are attracting a lot of attention in electrochemistry[1] and are one of the most fundamental physical systems used to study and understand nucleation and growth phenomena at solid-liquid interfaces.[2] In (electro-)catalysis or corrosion, NBs are frequently employed as nano-reporters that are associated to local catalytic activity.[3-5] NBs can constitute intermediate states that further grow and merge into micro and macroscopic bubbles. Through the creation of a third phase sandwiched between the electrode and the solution, bubbles also deactivate electrocatalytic materials and are therefore responsible for substantial current drops,[6] which is detrimental for devices efficiency. Both reactivity reporting and detrimental effect in devices efficiency motivate the needs of studying them at the single object level.

Recently, nanoelectrochemistry has proved to be a means of choice to probe the electrochemical (EC) nucleation and growth of single NBs as it allows both triggering their appearance and analyzing their behavior, through the abrupt current decrease they provoke.[6-9] The use of nanoelectrodes or nanopipettes and current amplifiers notably permitted to determine, *in situ*, the critical nuclei size, geometry, nucleation rate, activation energy and lifetime of electrochemically generated NBs. Nanopipettes have also been used in Scanning ElectroChemical Cell Microscopy (SECCM) configuration to image the distribution of NBs nucleation sites on large electrode through the hopping of an attoliter EC cell.[10,11] However, these strategies are often limited to model systems (disk electrodes as an example) and to the

study of single entities without considering the whole EC process and the effect of the growth of neighbouring NBs.

An alternative to reach single-entity resolution from an ensemble of active sources is to separate them in space, by combination with high spatial resolution imaging techniques.[12,13] It has been achieved by employing scanning probe microscopies (SPM), such as *in situ* Atomic Force Microscopy (AFM), possibly coupled to an EC actuation, that provided evidences of stable surface NBs.[14-16] The latter technique allows imaging *in situ* both the density of NBs and their dimension (height and footprint diameter). This provides a quasi-3D visualization of the NB which complements a Faradaic analysis of the electrochemical charge. However this is achieved within a limited $\mu m^2$ imaged field and at rather low imaging throughput, and in addition the tip scanning affects the NB morphology. *In situ* transmission electron microscopy (TEM) also allowed probing sub-100 nm NBs next to cathode materials. It allows inferring the 3D shape of the NB over the electrode surface, though the requirements of thin liquid cells strongly affects the NB growth dynamics which is also strongly influenced by radiolysis effects from the electron beam.[17,18]

Optical microscopies provide pertinent imaging alternative in term of high throughput and wider field of observation. Recently, the dynamics of EC single NBs formation was optically monitored by Total Internal Reflection Fluorescence Microscopy (TIRFM).[19,20] By tracking local intensity changes in optical images taken during a cyclic voltammetry experiment, it was possible to infer the contribution of hydrogen spillover, effective even on non-reducible support,[21] induced by HER on gold nano-plates electrocatalysts. However, this approach requires a luminescent label and hardly images the (nano)materials at the origin of the NBs. If this origin is metallic NPs supporting localized surface plasmon (LSP), they can be imaged directly under

dark field illumination.[22-24] Meanwhile, one can exploit the sensitivity of the LSP resonance to local charge and refractive index variations to identify, from individual NP extinction spectra, the role of $H_2$ spillover before NB formation.[25] NBs can also be visualized directly, without label, by optical microscopy operated under dark field illumination[3] or by employing the plasmon-based TIR imaging of surface plasmon resonance microscopy (SPRM).[26,27] Both label free techniques have the further advantage of being able to visualize the NP at the origin of the NB production.

So far, the *operando* imaging of <30nm NPs, even for plasmonic materials, is challenging. One possibility, proposed by our group,[28-30] to push such detection is to rely on Interference Reflection Microscopy (IRM), a highly sensitive label-free technique used in biology studies,[31,32] which can be extended for electrochemical reactions to a large number of transparent[28-30,33] or opaque (reflecting)[34,35] substrate electrodes. Besides a good generality in substrate, IRM also allows imaging a wide range of nanomaterials: Ag NPs down to ca. 10 nm in diameter as well as non-plasmonic materials (*i.e.* weaker scattering objects).[34,36] Herein, such microscopy is used to probe *operando* an ensemble of individual NPs and the surface NBs they generate under electrochemical activation. Taking advantage of the high spatial and high temporal resolution of such optical nanoscope, the position of both the nano-catalysts and the NBs are tracked dynamically. Moreover the modeling of the optical response of gas NBs in the IRM configuration allows evaluating dynamically the size and shape of the NBs during their production, enabling to discuss the growth mechanism of gas NBs from single catalytic colloidal Pt NPs. It is shown that the Pt NPs are rapidly electrically disconnected by the NBs, which are still continuously growing. The wide field of view of the microscope, through an *operando*

monitoring, allows discussing possible cross-talk effect during proton reduction at a disordered array of single Pt NP catalysts supported on an Indium Tin Oxide (ITO) electrode.

## RESULTS AND DISCUSSION

As shown in Figure 1a, the ITO electrode is used both as an optical sensor and as the working electrode (WE) of a ca. 200 µm diameter micro-electrochemical cell formed by an electrolyte droplet dispensed and held by a micropipette of ca. 100 µm diameter[37-39] positioned atop an inverted microscope. The backside of the ITO substrate is illuminated through a high numerical aperture objective (x63, NA = 1.4), and the reflected image of the interface between the ITO electrode and the electrolyte is recorded by the microscope camera. More specifically, on the recorded optical images, the optical signal ($I_{opt}$ defined in Figure 1c) is a combination (interference) of the field reflected by the electrode interface and of the far-field back-scattered by the NPs (see sections SI1 and 2 in the supporting information, SI). This interferometric mode imaging provides enhanced visibility of wide range of nanomaterials.[40] Platinum NPs were first drop casted on the ITO electrode and their catalytic activity was locally investigated by approaching the tip-end of a micropipette filled with sulfuric acid (5 mM) near the electrode surface. A typical cyclic voltammogram obtained at the NPs-supported ITO WE delimited by the electrolyte droplet is shown in Figure SI3 in SI. It evidences a reduction peak with a maximum recorded at -1 V followed by an oxidation peak at ~ -0.5V, whereas without NPs no current is detected at such potentials. It is characteristic of the catalytic reduction of $H^+$ followed by $H_2$ reoxidation at a large ensemble of Pt NPs. A droplet of the same electrolyte was positioned in another location of the NP supported ITO surface, and the electrode was biased, in a chronoamperometric experiment, CA, at a constant and sufficiently negative potential (-1 V *vs* Pt QRE) to ensure a mass transfer limited reduction of $H^+$ into $H_2$ at the Pt NPs, while both the

electrochemical current (see Figure 1b) and the optical images are recorded at a frequency of 500 Hz and 20 Hz respectively.

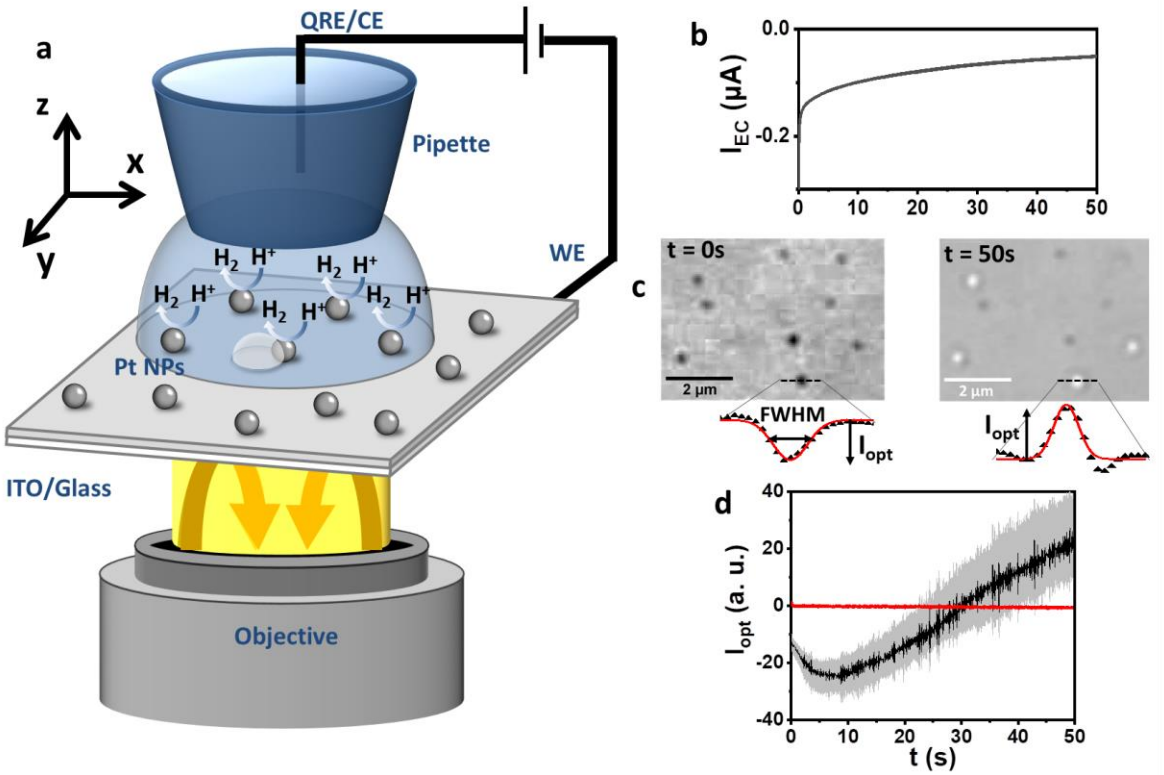


**Figure 1.** (a) Schematic representation of the opto-EC setup used to study HER at single 40 nm Pt NPs deposited on an ITO surface. (b) EC current recorded during a chronoamperometric, CA, experiment at the ITO surface polarized at -1 V *vs* Pt in 5 mM of sulfuric acid for 50 s. (c) Optical images before and after CA together with optical profiles along a line, in the same region, over a NP evolving later a NB. (d) Median (black), first and third quartiles (grey) of the variation of $I_{opt}$, defined in c, of N>100 NPs as a function of the electrode polarization time; background fluctuation in red.

The optical monitoring was performed in the center of the droplet within a ca. 55x40 µm² full image shown in Figure SI4a in SI. The dropcasting of the NPs produced, from coffee-ring effect, a heterogeneous density of NPs over the surface with in some areas, µm² large regions of agglomerated NPs. Apart from these large agglomerates, different regions of interest, ROIs, within the imaged field of view were used to apprehend the formation of $H_2$ at individual NPs.

Figure 1c shows a characteristic example of a zoom over a 30 µm² area of a ROI (see larger and magnified images in Figures SI4a and b in SI) of the optical image of the electrode populated by individual NPs and immersed at t=0. It contains dark contrast features resulting from the presence of the Pt NPs (see data analysis in SI). After 30 s of EC actuation, the contrast of few optical spots changes and becomes bright, while the intensity of the others ones as well as of the background remains fairly constant. Typical evolution of the background subtracted intensity variation at these spots, extracted following the procedure described in section SI4 in SI, is presented in Figure 1d while other ones in Figure SI4c in SI. Based on image sequences covering areas >250 µm² and containing N>100 Pt NPs (see those ROIs in Figure SI4a), 30% of the latter generate a significant optical intensity fluctuation during the 50 s of electrode polarization at -1 V. If the latter fluctuation is due to HER, it can then be concluded that all the NPs do not possess an equivalent catalytic activity, which is probed here optically. It could be due to discrepancies in surface functionalization by citrate capping agent, sporadic sulfate adsorption, the presence of an oxide layer that passivates the NP surface, or a poor connection with the current collector. To ensure that it is not related to NP aggregates that locally increase the HER electrode activity, the presence of aggregates was scrutinized by correlative *ex situ* SEM analyses.

As presented in Figure 2a, the SEM image in the same location as the optical images of Figure 1c reveals that the NPs are individual entities and are separated by a distance greater than the diffraction limit so that they are optically resolved. Over larger image areas, apart from the few NP µm large agglomerates (see section SI4 in SI), NPs are also mostly dispersed as individual entities or are present as small aggregates.

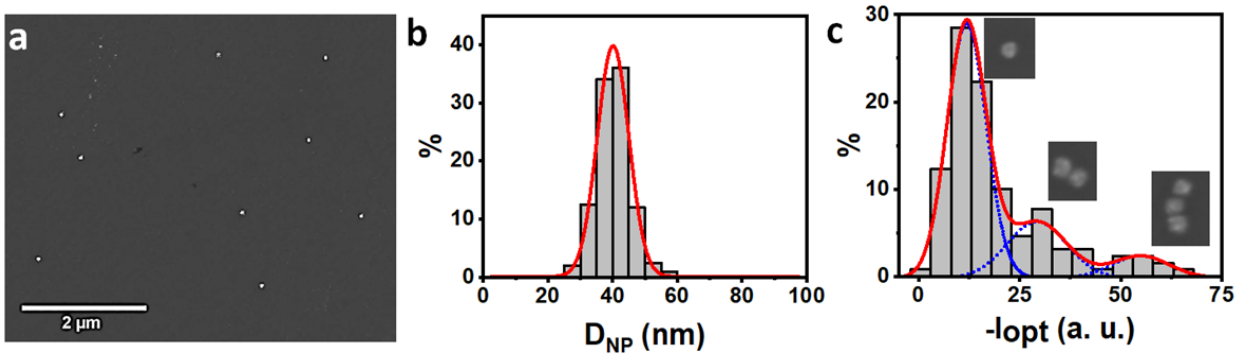


**Figure 2.** (a) SEM microscopy image of Pt NPs (same location as in Figure 1c) immobilized at the ITO electrode surface. (b) SEM deduced size distribution of the Pt NPs (N>200). (c) Distribution of the optical features intensity (N>200) obtained from one optical image. SEM images of NP monomer, dimer and trimer are incrusted in (c).

Based on SEM image analysis and the size distribution graph of Figure 2b, the mean NP size was estimated to 41±5 nm in diameter. In contrast to the narrow SEM size dispersion, the distribution of NP intensities, $I_{opt}$, in Figure 2c, presents a trimodal distribution having a major mode with maximum centered at $I_{opt}\approx$-11 representing 68% of the population and two additional modes representing respectively 23% and 9% with local maxima centered at $I_{opt}\approx$-28 and $I_{opt}\approx$-54. From same location SEM/optics imaging analysis of the different populations, the latter two modes correspond to NP dimers and trimers, as those imaged in SEM and shown in Figure 2c. If individual NPs within these aggregates cannot be spatially resolved optically, the aggregates can

be easily discriminated by measuring the intensity, $I_{opt}$, of the diffraction limited spots, as shown in Figure SI5 in SI. Based on this result, only the HER activity of the most abundant population (the individual Pt NPs) was investigated.

The changes in optical intensity at the location of NPs during HER are attributed to $H_2$ evolution. Indeed, a similar optical change is observed at µm large agglomerates but the same experiment performed in either a pH~7 (see section SI6 in SI) or a 0.2 mM $H_2SO_4$ droplet over the same NPs supported ITO surface or in a 5 mM $H_2SO_4$ droplet at an ITO surface (in the absence of Pt NPs), did not show any fluctuation of the optical intensity. If the earliest label-free imaging of HER at Pt NPs by SPRM suggested $I_{opt}$ changes were due to local molecular $H^+$ or dissolved $H_2$ concentration gradient around catalytic NPs,[41] we believe such change results from $H_2$ gas NB formation, as demonstrated later by White *et al*., who showed that single gas NBs can nucleate and grow from electrochemical reactions at nanoelectrodes.[6] The optical visualization of NBs on surfaces was further confirmed (i) from fluorescence imaging (rigorously of the NB-solution interface) during HER at electrode surface or NPs, or (ii) from label-free imaging of gas NBs, either by SPRM at heated surfaces[27,42] or dark field microscopy for qualitative benchmarking of NPs electrocatalytic activity.[3,43]

We explore here the possibility of analyzing quantitatively the NBs formation from the variations of the local optical intensity, $I_{opt}$, recorded by IRM. The optical transients of single NBs at single Pt NPs were extracted by computerized image treatment from the video recorded during the 50 s of the electrode polarization at -1 V *vs* Pt. The variation with the polarization time, t, of the median $I_{opt}$ value, as well as of its first and third quartile values, recorded over N>100 single NPs is presented in Figure 1d and compared to the background intensity. $I_{opt}$ decreases up to ca. 8 s and subsequently increases to the point of showing a contrast inversion

(features brighter than the background) at ca. t>25 s. These fluctuations are attributed to the formation of single surface NBs, pinned at individual Pt NPs during HER. For a NB to nucleate at an active site and then grow, there is first a condition for the local concentration of electro-generated molecular $H_2$ precursors, which should locally supersaturate the solution according to the classic nucleation and growth theories, *e.g.* following the Epstein-Plesset theory.[44] This is likely occurring at the most reactive NPs, which ensure the highest local $H_2$ concentration at the earliest stage of the EC actuation. In this respect, the footprint of a NB formation is expected to reveal the most active region of an electrode, or here the most active Pt NPs. The production of NBs at only a fraction of the NPs may, at first sight, indicate that only this fraction of NPs is active.

Noteworthy, the EC current trace recorded in the CA experiment (Figure 1b) suggests the electrolyte droplet is saturated by $H_2$ during the whole experiment, at least in the optically imaged area. Indeed, the $H^+$ reduction current density, estimated from the CA curve assuming a 200 µm diameter electrolyte droplet, steadily decreases from ca. 0.76 mA/cm$^2$ at the start of the CA to 0.16 mA/cm$^2$ at t=50 s. The pseudo steady current at long times suggests a pseudo constant flux of $H_2$ production. If NPs were considered as independent individual nanosources of $H_2$, *e.g.* nanoelectrodes, within t>1s each one should operate under steady-state $H_2$ hemispherical mass transfer regime. However, 40 nm nanosources cannot be considered as independent when separated by < 10 µm.[45,46] Both the inter-NP and inter-NB distance distributions, given in Figure SI4d in SI, are below 5 µm, suggesting the occurrence of $H_2$ diffusion cross talk between NPs. As it will be discussed below, the dynamic tracking of the dimension and position of each NB during its growth suggests that most nanosource NPs are rapidly switched off by the NB they generate. The continuous growth of the NBs must then be sustained from other cross-talk

sources. The µm large coffee-ring agglomerates sporadically distributed over the ITO surface resulting from the drop casting of the Pt NPs are likely such sources of $H_2$ homogenization over the ITO surface. Typically, in the 55x40 $\mu m^2$ region (Figure SI4a) optically monitored within the electrolyte droplet, 3 of them are clearly detected, which all show an optical intensity variation and then $H_2$ gas evolution during the CA experiment. If the catalytic activity of these agglomerates is not discussed herein, from the same computation arguments,[45,46] such HER active agglomerates are expected to afford after few seconds and over a much wider region (several tens of micrometers) a homogeneous $H^+$ and $H_2$ concentration over the ITO surface. This implies they will sustain a local saturation of the solution by $H_2$ homogeneously over the ITO surface, and therefore conditions for sustaining a long time growth of $H_2$ bubbles.

After few seconds both $H^+$ and $H_2$ diffusion is then operated through a linear diffusion regime, along the vertical z-axis, from the electrode surface to the micropipette opening. The expansion of the $H^+$ and $H_2$ diffusion layer along the vertical axis explains the current density decrease with time. Owing to the finite geometry of the droplet, this current decrease corresponds to the exhaustive electrolysis of $H^+$ into $H_2$, enforcing a saturation of the droplet by $H_2$. This saturation is further attested by the high stability and the unusually long lifetime of the NBs. Such stability is verified here by optical monitoring through the >140 s long NBs dissolution time (see examples in section SI7 in SI) after the CA was stopped. [2,47]

As in the first instant of the NB growth the NP signal dominates, the optical transients, $I_{opt}(t)$ in Figure 1d, recorded during HER were subtracted from the signal related to the NPs, as proposed by Zhang and co-workers from a first approximation of additive NP and NB contributions and briefly recalled in section SI1 in SI,[4] allowing to depict the NB growth. To rationalize such NB growth from the interferometric optical images of NBs at an ITO aqueous solution interface were

modelled by boundary element method, as previously discussed[34,36] and detailed in section SI2 in SI. NBs grow from surfaces as spherical caps characterized by two geometrical parameters defined in Figure 3a, namely, D the diameter of the footprint of the NB on the surface and $\theta$ the contact angle formed with the electrode surface and measured through the gas phase. The volume of such spherical cap NB is given by:

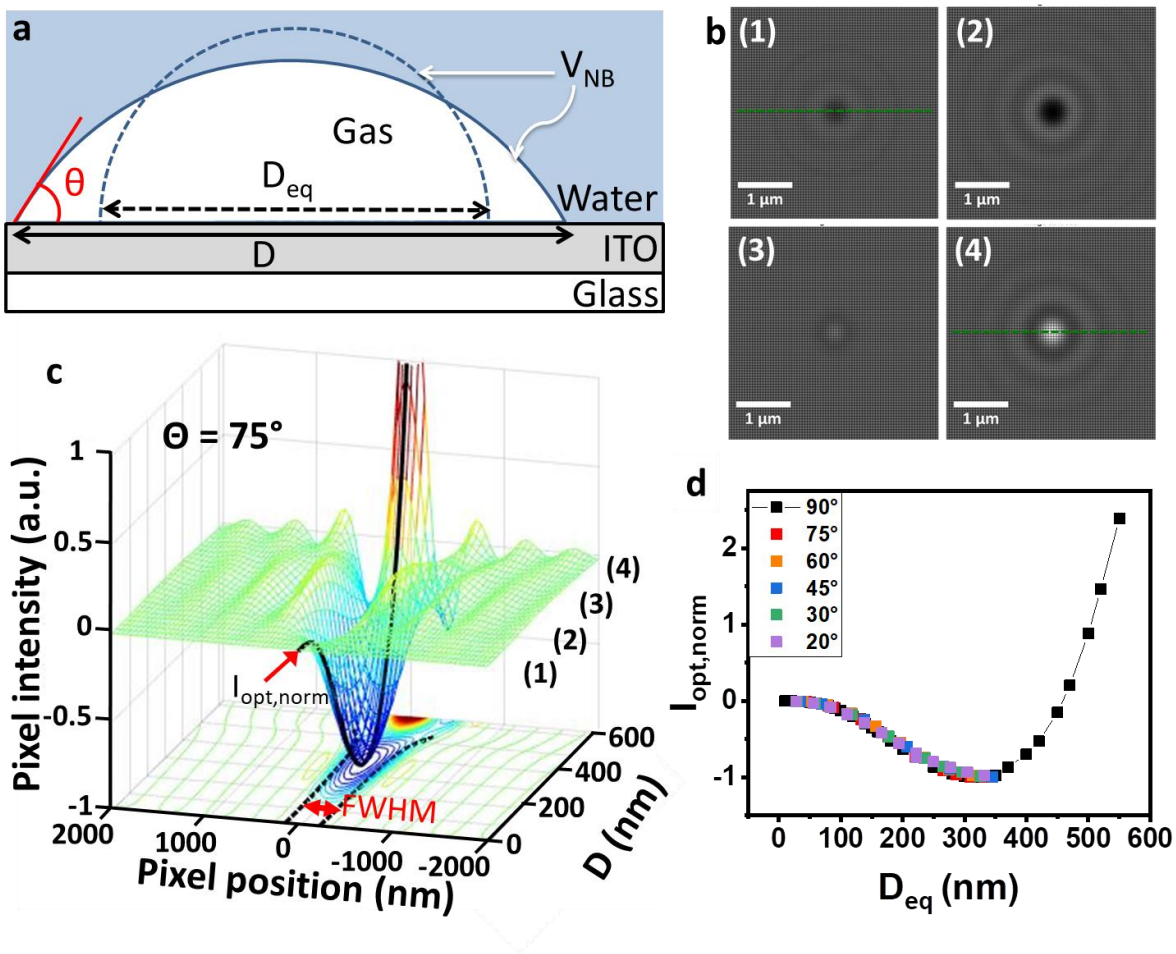


**Figure 3.** (a) Schematic representation of the optically simulated configuration: a NB sphere cap surface is generated at the interface between the glass coated ITO electrode surface and an aqueous electrolyte. The NB sphere cap is defined by the diameter and contact angle (D, $\theta$) of its footprint on the ITO, and by an apparent diameter, $D_{eq}$, of an equivalent (dashed) hemisphere

with same volume, $V_{NB}$. (b) Simulated optical images of hemispherical NBs of different sizes (127, 238, 373, 412 nm, from 1 to 4) located on top of an electrode (70 nm thick ITO layer). (c) Theoretical variation of optical intensity profile along cross section (*e.g.* dashed green lines in b) as a function of the NB diameter, D, showing the variations of $I_{opt}$ (black line) and FWHM (dashed black line) with D; $\theta = 75°$. (d) Evolution of $I_{opt}$ as a function of $D_{eq}$ for a single NB for contact angles ranging from 20° to 90°.

$$V_{NB}=\frac{\pi}{24}\frac{D^3}{sin^3\theta}(2+cos\theta)(1-cos\theta)^2 \qquad (1)$$

so that the geometry of a NB is fully determined by only 2 independent parameters among D, $\theta$ and $V_{NB}$. Henceforth, for the sake of dimension homogeneity, one defines an apparent NB size, $D_{eq}$, as a descriptor of the NB volume,

$$D_{eq}=\left(\frac{12}{\pi}V_{NB}\right)^{1/3} \qquad (2)$$

which corresponds, for a given NB volume, whatever D and $\theta$, to the diameter of the hemisphere, dashed in Figure 3a, having the same volume $V_{NB}$ as the original spherical cap. It ensues from (1) and (2) that for $\theta$=90°, $D_{eq}$=D. Henceforth, the geometry of a given NB is now fully determined by only 2 independent parameters among D, $\theta$ and $D_{eq}$.

The theoretical optical images were then computed for NBs of various volumes, meaning for various couples of D and $\theta$ values. The examples of theoretical images in Figure 3b for hemispherical NBs and for NBs with smaller contact angle (not shown) present the same general trends: small NBs appear as negative contrast features in the center of the calculated images and the larger the NB the darkest the feature (*e.g.* for hemispherical NB of diameter D<250 nm). This trend is reverted as the optical contrast feature is becoming brighter for further NB increase, until the NB can be observed as bright contrast feature (*e.g.* for D>380 nm for hemispherical NBs). In

a first approximation and following the methodology used in Figure 1c for experimental contrast features, the modeled contrast features were fitted by a Gaussian peak characterized by its intensity $I_{opt}$ (the equivalent of the experimental $I_{opt}$ values) and its full width at half maximum, FWHM.

As both D and $\theta$ influence the $I_{opt}$ and FWHM characteristics (see Figure 3c,d and section SI8 in SI), for the sake of simplicity, we first consider that NBs grow with constant contact angle. The hemispherical case $\theta$=90° was first chosen based on the macroscopic evaluation of the contact angle $\theta_M$=90° of water droplets or gas bubbles in water on the ITO surface (see section SI9 in SI). The theoretical normalized $I_{opt}$ variations as a function of $D_{eq}$ (note that $D=D_{eq}$ for $\theta$=90°) are presented in Figure 3d. The calculations not only reproduce the contrast inversion but also the minimum of intensity observed in the experimental optical transients of Figure 1d.

Figure 3d also overlays the $I_{opt}$-$D_{eq}$ variations for other contact angles $90°>\theta\geq20°$. The good overlap of these variations for small enough NBs, $D_{eq}$<350 nm, demonstrates that $I_{opt}$ only depends on the NB volume for $V_{NB}<1.6\text{x}10^{-2}$ µm$^3$. One can use such quantitative simulation of $I_{opt}$–$D_{eq}$ variations to extract, from the experimental optical transients, the dynamics of NBs growth without prior knowledge of the real NB geometry. It is illustrated in Figure 4a, where an $I_{opt}$ transient is transformed, into an apparent growth curve ($D_{eq}(t)$) for a single NB appearing over a single NP region, by inversion of the modelled $I_{opt}$–$D_{eq}$ curve from Figure 3d.

The amount of $H_2$ gas contained inside such a NB, $n_{H2g}$, was then estimated from both the NB volume and the gas internal pressure, $P_{gas}$, assuming an ideal gas,

$$n_{H2g}=V_{NB}\,P_{gas}/k_BT \qquad (3)$$

where $k_B$ is the Boltzmann constant and $T$ the temperature, while the internal pressure is obtained from the Young-Laplace equation:

$$P_{gas} = P_0 + \frac{4\gamma \sin\theta}{D} \qquad (4)$$

with $P_0$=1 atm, the ambient pressure and $\gamma$=72.8 mN/m, the aqueous solution surface tension. For the case of a hemispherical NB, $\theta$=90°, $D_{eq}$=D and $P_{gas}=P_0+4\gamma/D$.

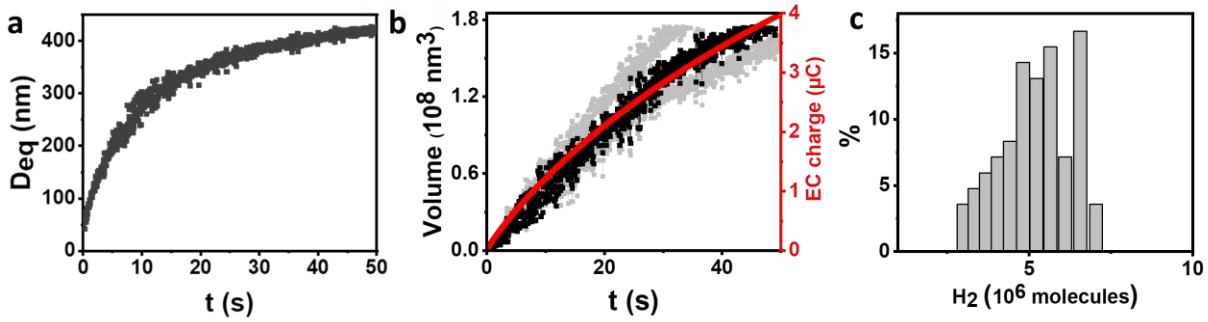


**Figure 4.** (a) Evolution of the apparent size of a single NB generated at a single NP as a function of time. (b) Correlation between the NB volume (median in black, first to third quartile in grey) and the measured total EC charge (in red). (c) Distribution of the estimated amount of hydrogen molecules inside single gas NBs after 30 s of EC actuation.

The latter equations then allow a quantitative estimate of $n_{H2g}$ along the CA experiment at the single NB level. As in electrodeposition processes, it can be compared to the overall electrochemical charge exchanged for the electro-generation of nanomaterials at an electrode surface. This was indeed evidenced for NB growth on longer timescale allowing an *in situ* AFM monitoring.[15] Such growth dynamics fits with the Epstein-Plesset theory for gas NB growth.[44] It is further confirmed here by a $t^{1/2}$ growth law during the first ~20 s (Figure SI10 in SI). More pertinent from the point of view of the Faradaic yield of the electrochemical reaction, the plot of Figure 4b shows that the average NBs volume (roughly equivalent to $n_{H2g}$ since for $t$>3 s, $P_{gas}$≈7±1 atm) correlates to the charge passing through the EC cell. Finally, one can also

construct a distribution of the amount of hydrogen molecules trapped in single NBs at any arbitrary time of the EC experiment and at high throughput.

Such a quantification, illustrated in Figure 4c for N>100 single NBs formed after 30 s of EC actuation, is interesting for benchmarking, since it provides a quantitative mapping of the catalytic activity of individual NPs towards HER, as qualitatively suggested earlier.[3,43] Owing to the strong interaction of $H_2$ gas with Pt NPs, it is expected that the latter act as nucleation sites for $H_2$ NB growth. At first sight, it seems also reasonable that the most catalytically active NPs produce the highest $H_2$ local concentrations and therefore grow NBs. As a further information brought by such quantitative analysis, the limit of optical detection, L.O.D., of gas NB was evaluated, in terms of equivalent diameter, to $D_{lod,eq}$ ~ 50 nm, yielding for $\theta$=90° a L.O.D of ~$5x10^4$ $H_2$ molecules, a sensitivity equivalent to that of SPRM.[42]

A closer examination of the theoretical images, at constant contact angle, shows that the FWHM of the dark contrast features also varies with the NB footprint D. Figure 3c presents the cross section of the predicted contrast features for different D values and a constant contact angle of 75°. The values of the FWHM extracted from these cross sections are reported in the lower plane of Figure 3c and in section SI8.b in SI. Interestingly, the variations of the FWHM with *D* hold whatever the NB contact angle, as long as it is detected as a dark feature and roughly as long as $I_{opt}$ is sufficiently different from the background (sufficient signal to background ratio, *i.e.* D<500 nm in Figure 3c). It suggests that the footprint diameter variation, ΔD, can be extracted from such diffraction patterns for NBs with 200-250nm < D < 500nm. Noteworthy, the lower bound value is actually consistent with the value of the point spread function PSF≈1.22 λ/2NA≈220 nm of the modeled microscope with objective's numerical aperture, NA=1.4, and detection wavelength λ=510 nm.

Experimentally, the FWHMs of the optical patterns were then obtained from a dynamical super-localization approach (a Gaussian fitting of the PSF, see Figure 1c) during the growth of individual NBs (*i.e* while $I_{opt}$ varies). Examples of such FWHM variations (see section SI11 in SI) during the CA experiment for N=10 NBs, indeed show an increase of the FWHM for t>2 s. These variations attest that, as soon as t>2 s, the NB footprint diameter, *D*, is above the ca. 250 nm of the microscope PSF.

Therefore, from the same strategy as that used for $I_{opt}$, the experimental evolution of ΔD of an individual NB during its growth was inferred from the experimentally measured ΔFWHM along the CA experiment, with the help of the predicted FWHM-D curve (see section SI12 in SI).

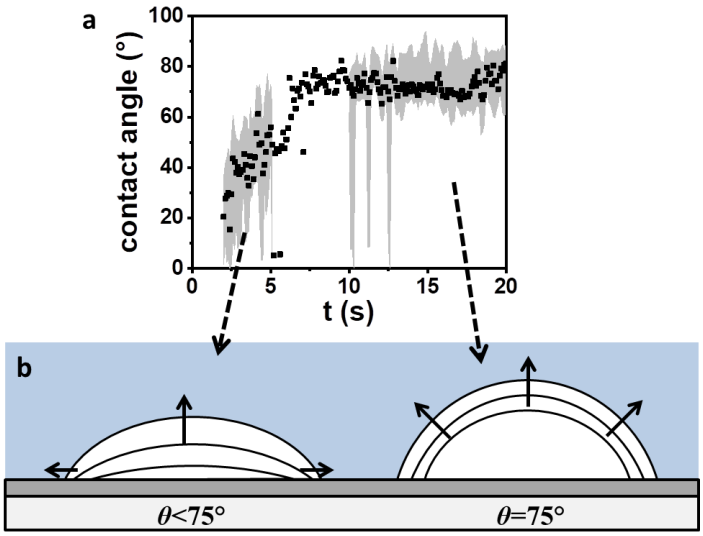


**Figure 5.** (a) Single NBs contact angle variations (N=12, median and first to third quartiles in black and grey, respectively) estimated from $D_{eq}/D$. b) Schematic representations of the two NBs growth regimes at short and long times (with an increase of the contact angle or at constant contact angle).

Overall, such inspection of the optical model then suggests that the monitoring of both FWHM and $I_{opt}$ of the optical feature yields two complementary information, respectively the footprint,

*D*, and the volume of the NB, $V_{NB}$ (or equivalently $D_{eq}$). From equations (1) and (2), it can be shown that the $D_{eq}/D$ ratio is a decreasing function of $\theta$, allowing then from both independent and complementary optically inferred parameters to evaluate the NB contact angle on the surface (see section SI12 in SI). This analysis was tested on the experimental optical images at the early stage (t<20 s) of a NB growth. The resulting variation of the evaluated NB contact angle is shown in Figure 5a.

The trend in Figure 5a, for N=12 NBs, demonstrates that the NB grows according to two growth regimes schematized in Figure 5b. The NB contact angle increases from ca. 30° to 75° during the earliest stages of the NB growth. Later, the NB mostly grows at a constant contact angle of 75° by an increase of its footprint on the surface. These observations of growth modes with increasing contact angle agree with current theories on NB nucleation and growth.[2,48]

Indeed, formally, owing to the intervention of the gas internal pressure in (3), the growth dynamics of gas NBs on surfaces differs from that of solid NPs. If the latter most often operates at constant contact angle, it is less likely for gas NBs, which could be pinned to surfaces enforcing a growth at almost constant footprint on the surface while the contact angle of the NB increases at the first instants of the growth.

Our results agree with the previous AFM imaging of NB growth/dissolution processes,[15] and the later theories proposed to explain that at the nanoscale, the contact angle of gas NBs decreases with decreasing NB size.[2,48] There is a further energy minimization argument, as with a small contact angle during its nucleation stage, a NB presents a radius of curvature, $r_{curv} = D/2\sin\theta$, much larger than its footprint on the surface, *D*. It allows, based on (4), the NB to nucleate and grow with a considerably decreased gas internal pressure.

The smallest NB contact angle that could be evaluated here (25-30°) strongly suggests that NBs may nucleate on surfaces with smaller contact angle than their macroscopic value. Moreover, contact angles as low as 24-34° for <10 nm $H_2$ nucleating NBs at Pt surface have recently been reported.[9,11] Taking into account that macroscopically, Pt has a wettability comparable to that of ITO ($\theta_M$=90°), the contact angle values are also in agreement with those reported herein.

However, the measured NB footprint is significantly higher (D up to 300 nm) for $\theta$=30° in the present work than the reported 10 nm nuclei on Pt nanoelectrode. This difference might be explained by the difference of $H_2SO_4$ concentration used (5 mM herein *vs* >1 M in other works). Indeed, at best, the mass transfer limited reduction of the 5 mM $H_2SO_4$ solution would provide a growth of NBs with a maximum 5 mM concentration of dissolved $H_2$. From Henry's law describing the equilibrium between the saturation of the solution at the NB surface, $C_{H2,s}$, and the internal $H_2$ NB pressure through Henry's constant $K_{H2}$=0.78 mM/atm:

$$C_{H2,s}=P_{gas}K_{H2} \quad (5)$$

the 5 mM upper limit of dissolved $H_2$ imposes an upper limit for $P_{gas,M}$= 7.4 atm in the NB during the whole CA experiment, much lower than those employed at higher concentration during single NBs electro-generation at nanoelectrodes.[6-11,49] It imposes from (4) a nucleation and growth of NBs with lower bound curvature radius $r_{curv,m}$=266 nm. Typically, within the reported values of ca. $\theta$~30° contact angle, the smallest NB nucleus that could be produced under our conditions should then be a spherical cap of footprint diameter $D=2r_{curv}\sin\theta$=266 nm, a value close to those reported experimentally, and height $h=r_{curv}(1-\cos\theta)$=35 nm. The consistent predicted and observed dimensions (D and θ) of the NB in its earliest optical detection support

that IRM provides a pseudo-3D analysis of such dynamic process, as would do AFM,[14,15] but at a higher throughput and image acquisition rate, and without possible tip-NB contact perturbation.

The optical detection of the NP, along with the NB, prevents a sensitive detection of the first instant of the NB nucleation, which usually takes place within < 100 ms.[9,27] However, the optical imaging further allows mapping $H_2$ evolution at the NP supported ITO. Figure SI13 in SI provides a map of the characteristic time needed to grow individual $D_{eq}$=350nm NBs within different ROIs and for N>100 NBs. These characteristic times are widely distributed, as the $n_{H2}$ estimated at 30 s in Figure 4c, and range between 2 and 15 s, though with no apparent dependence on spatial localization: they are neither related to the proximity of a neighbouring NP or NB or to the µm large agglomerates. Such variability is then mostly related to the NB nucleation, which has different origins, relative to either the gas nucleation activation barrier or the electrochemical process activation barrier. The importance of nucleation activation barrier has been modelled or experimentally measured for the nucleation of NBs of different gases at nanoelectrodes[9] or under thermal activation at SPR surfaces.[27] Although the nucleation of NBs occurs on the sub-100 ms range, not explored here, gas nucleation rates for mass transfer limited electrochemical processes show a much narrower (less than few %) distribution than the growth times experimentally observed here. The wider distribution observed here could be related to the influence of the surface roughness and/or chemistry of the NP or ITO on the nucleation activation barrier (*i.e.* the wetting of the NP).[27] Surface chemistry could play similarly a significant role in the overall electrochemical activity of the NP. The capping agent of the NP is expected to control both the electrical contact between the NP and the electrode and the electron transfer rate for HER at the NP-solution interface. Recent works have also demonstrated the importance of the control of NP-electrode contact resistance in single entity electrochemistry.[50]

Considering these latter effects predominate, the NB growth activity suggests that the $H_2$ NBs nucleation occurs at first on Pt NPs, which possess higher apparent activity toward proton reduction. It is then tempting to suggest that the most active NPs will grow the largest NBs.

However, owing to the 3D optical reconstruction of the NB during its growth, the geometrical situation is schematically depicted, at scale and considering a slight off-centering of the NB and the NP, in Figure 6a and b for different instants of the growth of a NB, employing the contact angles evaluated in Figure 5a. It can be concluded that during the NB growth, the NB may cover the whole NP, disconnecting it from the electrolytic solution, typically for t > 3-5 s. The catalytic reaction may then be halted and the NB should stop growing, unlike what is observed in Figure 4a.

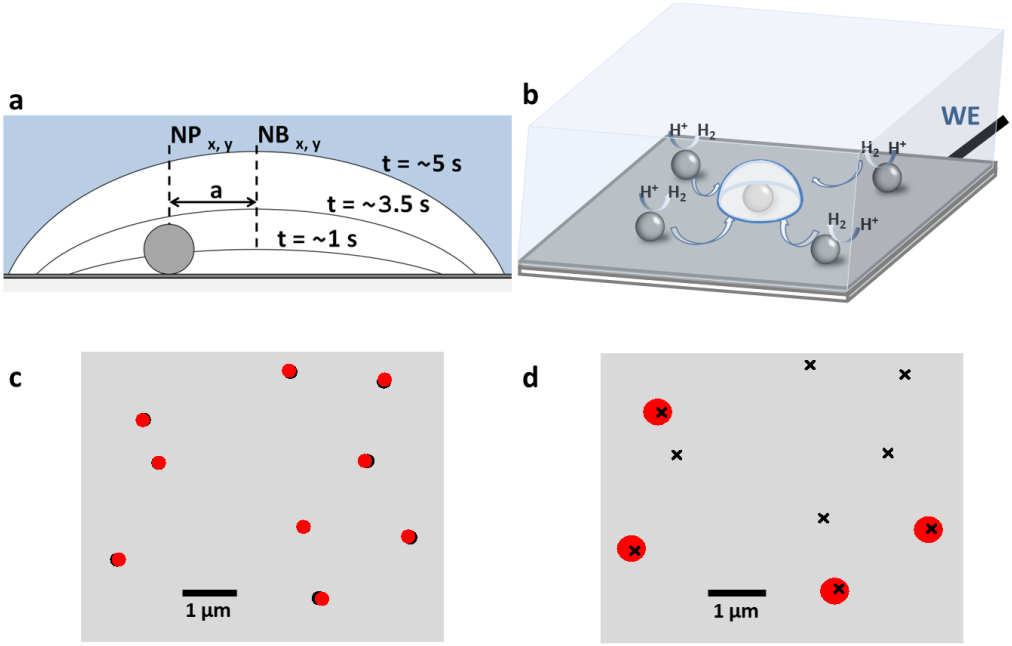


**Figure 6.** (a and b) Two schematic representations (side and perspective view, respectively) of a $H_2$ NB disconnecting a Pt NP during HER. (c) Pt NPs positions located by Gaussian fits before (black dots) the NBs generation and after (red dots) the complete NB dissolution. (d) Pt NPs positions before the electrode polarization (black crosses) and $H_2$ NBs positions (the red disks

represent to scale the electrode area covered by the NBs) after 50 s of EC actuation. The electrode region is the very same as that presented in Figures 1c and 2a.

One possibility though to prevent the NP disconnection could be that the NP is pinning the NB and both are strongly off-centered. Because IRM is label-free, both the NP and NB can be detected separately. Their respective positions over the reaction were also monitored by super-localization, as illustrated in Figure 6c and d for the very same electrode region shown in Figures 1c and 2a. We used the same dynamical super-localization approach to record the precise location of the centers of mass of the Pt NPs in the absence of NB. Subsequently, when the NB signal dominates (dark or bright) its center of mass is located by employing the post-treatment proposed by Zhang and co-workers and mentioned above.[4]

The possible alteration of the electrode nanostructure caused by the EC actuation was first investigated by comparing the NPs positions before the NBs nucleation and after their subsequent dissolution (black and red dots in Figure 6c, respectively). According to Figure 6c, most NPs are weakly bonded to and migrate through the ITO surface, 40 nm in average, the tracking precision being ~10 nm.[36] Even if the NP motion could be induced by the electrode polarization, recent works suggest that it would be due to non-uniform chemical fluxes generated during the EC reaction at the NPs surface.[51] It could also be related to asymmetric NBs growth at the side of the NPs, propelling them by the same mechanism as for micro-motors.[52-54] After 50 s of actuation, the center of mass of the NBs detected in the same area as in Figure 1c (N=4 NBs with N=9 NPs) are located within an average perimeter estimated to <70 nm starting from the center of mass of their corresponding NPs. NPs and NBs are represented to scale as black crosses and red disks respectively in Figure 6d. NBs have also been found to be roughly stationary

during the growth, as no significant lateral motion is measured during the time scale of the EC experiment.

Therefore, owing to this short-range motion of the nucleating NPs, summarized in Figure 6c, NBs should disconnect the Pt NPs once entirely covering them at t=~3.5 s. However, no sharp EC current drops are observed in the EC current-time transients, while NBs continue growing. This observation could be explained by the $H_2$ feeding from other neighbouring sources. Solution or surface diffusion of $H_2$ could be equally invoked, the latter corresponding to the spillover, recently imaged on ITO surface by TIRFM visualization.[19]

Once the surface of the catalysts is saturated, the growth of NBs remains possible even if the catalyst is isolated from the solution by the covering NB, fed by the other non-blocked Pt catalysts, including the µm large agglomerates. Indeed, the NPs remaining apparently optically inactive can produce $H_2$ that diffuses in solution or hydrogen atoms that migrate out onto the ITO surface toward the existing NBs as schematized in Figure 6b. Through such phenomena, NBs can continue growing, even if the (most active) catalysts are rapidly electrically isolated. The EC current transient suggests an exhaustive electrolysis of $H^+$ and therefore saturation of the droplets by $H_2$ over the whole experiment duration. This means that the non-nucleating NPs and the presence of other large agglomerates would strongly contribute to such $H_2$ production, while the activity of the former cannot be probed optically here. Noteworthy some of these optically inactive NPs are also subjected to motion, which could suggest their electrochemical activity. This points to the necessity of complementary or multi-correlative electrochemical microscopies for deeper insight. Definitely, local electrochemical probings,[55,56] operated at the nanoscale, as those using nano-electrochemical cells, nanoelectrodes or nanopipettes[57,58] would allow unveiling such aspect.

## CONCLUSIONS

In (electro-) catalysis, NBs are frequently employed as nano-reporters that have been associated to the presence of local catalytic activity.[3,4] Together with their detrimental effect in devices efficiency, it motivates the needs of studying them at the single object level. Herein, the nucleation and growth of single surface NBs during electrocatalysis on single Pt NPs adsorbed on ITO electrode have been analyzed through IRM/EC coupling. Thanks to a SEM/IRM correlative microscopies approach, it is first evidenced simply through NPs optical intensity measurement that such a phenomenon can be quantitatively investigated selectively on a specific population of NPs, exemplified here from individual Pt NPs. With the help of optical images simulation, single NBs growth was quantitatively followed through the evolution of both the optical intensity and super-localization of the diffraction pattern associated to the NB optical image. With a sensitivity close to $5x10^4$ $H_2$ molecules, gas NBs were imaged, in pseudo-3D owing to the estimation of the footprint, the volume and the contact angle of the NB. The high throughput analysis of the growth process also revealed its correlation with the EC charge. In addition, the dynamic super-localization approach of both the NBs and the NPs evidences i) the possible, yet slight, *operando* nanoscale motion of the Pt NPs and, ii) the rapid electrical disconnection of a substantial amount of Pt NPs provoked by the NBs growth. Still, the NBs growth was continuously tracked even after the most active Pt NPs have been covered, strongly suggesting the presence of hydrogen crosstalk from less active NPs to the most active ones.[25]

## METHODS

## Materials

Citrate capped Platinum NPs dispersed in aqueous 2 mM sodium citrate were purchased from Nanocomposix® and used as received. The full characterization of the NPs including TEM images is available in the manufacturer website. Sulfuric acid of analytical grade was purchased from Merck®. Micropipettes were fabricated in-house by pulling 1.0 mm/0.5 mm borosilicate glass capillaries (outer and inner diameter, respectively) with a P2000 laser puller from Sutter Instrument®. The pipettes were polished on aluminum oxide tape (3 µm) and washed thoroughly with ultrapure water before use. Indium-Tin-Oxide coated coverslips with a resistivity of 70-100 ohms were purchased from SPI® and were carefully cleaned with ethanol and dried under argon flux before NPs deposition by drop casting from a colloidal solution.

## Opto-electrochemical instrument

The ITO coated coverslip was mounted on an inverted microscope (Zeiss Axio Observer 7) and was illuminated from the backside by a non-polarized white LED through a 63x oil immersion objective (Zeiss Plan Apochromat, numerical aperture of 1.4). The reflected light was collected by the same objective and directed to a CMOS camera (IDS®) operating at 20 frames per second. Typical optical images are made of 1000x700 pixels of 55 nm each, corresponding to a ca. 2117.5 $\mu m^2$ imaged region of the 200 µm diameter disk ITO surface contacted by the electrolyte droplet. The ITO surface was employed as a working electrode in a two-electrode configuration. The counter/quasi-reference electrode was a Pt wire inserted into the pulled micropipette. The latter was filled with sulfuric acid and the droplet located at the opening of the pipette was approached close to the ITO surface with the help of a 3 axis micro-controller to

form the electrochemical cell. The whole set-up was placed on a vibration isolation workstation to reduce mechanical noise. The opto-electrochemical measurements were performed using a CHI760 potentiostat with a sampling rate of 1 kHz and a bandwidth of 0.5 kHz. The potentiostat was synchronized with the CMOS camera by a signal generator.

**SEM imaging**

The electron microscopy images were recorded using a SUPRA 40 SEM-FEG scanning electron microscope from Zeiss®. A tension of 3 kV was used to acquire images. For same location microscopy analyses, the ITO surface was marked prior to NPs deposition.

ASSOCIATED CONTENT

**Supporting Information**.

The Supporting Information is available free of charge online on the ACS Publications website.

Experimental details, principle of IRM and BEM calculations, electrochemical experiments, optical intensity transients and optical images, same location SEM analysis, control experiments, NBs stability over time, simulated variation of $I_{opt}$ and FWHM, macroscopic contact angle measurement, experimental variation of FWHM, contact angle estimation and optical map of NB growth rates (PDF)

AUTHOR INFORMATION

**Corresponding Author**

Frédéric Kanoufi – Université de Paris, ITODYS, CNRS, F-75006 Paris, France; orcid.org/0000-0002-9784-2380; Email: frederic.kanoufi@univ-paris-diderot.fr

**Authors**

Jean-François Lemineur – Université de Paris, ITODYS, CNRS, F-75006 Paris, France.

Paolo Ciocci – Université de Paris, ITODYS, CNRS, F-75006 Paris, France.

Jean-Marc Noël – Université de Paris, ITODYS, CNRS, F-75006 Paris, France.

Hongxin Ge – Université de Paris, ITODYS, CNRS, F-75006 Paris, France.

Catherine Combellas – Université de Paris, ITODYS, CNRS, F-75006 Paris, France.

**Author Contributions**

The manuscript was written through contributions of all authors. All authors have given approval to the final version of the manuscript.

**Notes**

The authors declare no competing financial interest.

ACKNOWLEDGMENTS

P.C. and F.K. acknowledge funding from the European Union's Horizon 2020 research and innovation program under the Marie Skłodowska-Curie MSCA-ITN grant agreement no. 812398, through the single-entity nanoelectrochemistry, SENTINEL, project.

REFERENCES

[1] Ranaweera, R.; Luo, L. Electrochemistry of Nanobubbles. *Curr. Opin. Electrochem.* **2020**, 22, 102-109.

[2] Lohse, D.; Zhang, X. Surface Nanobubbles and Nanodroplets. *Rev. Mod. Phys.* **2015**, *87*, 981-1035.

[3] Li, S.; Du, Y.; He, T.; Shen, Y.; Bai, C.; Ning, F.; Hu, X.; Wang, W.; Xi, S.; Zhou, X. Nanobubbles: An Effective Way to Study Gas-Generating Catalysis on a Single Nanoparticle. *J. Am. Chem. Soc.* **2017**, *139*, 14277-14284.

[4] Zhang, T.; Li, S.; Du, Y.; He, T.; Shen, Y.; Bai, C.; Huang, Y.; Zhou, X. Revealing the Activity Distribution of a Single Nanocatalyst by Locating Single Nanobubbles with Super-Resolution Microscopy. *J. Phys. Chem. Lett.* **2018**, *9*, 5630-5635.

[5] Zwaschka, G.; Nahalka, I.; Marchioro, A.; Tong, Y.; Roke, S.; Campen, R. K. Imaging the Heterogeneity of the Oxygen Evolution Reaction on Gold Electrodes *Operando*: Activity Is Highly Local. *ACS Catal.* **2020**, *10*, 6084-6093.

[6] Chen, Q.; Luo, L.; Faraji, H.; Feldberg, S. W.; White, H. S. Electrochemical Measurements of Single $H_2$ Nanobubble Nucleation and Stability at Pt Nanoelectrodes. *J. Phys. Chem. Lett.* **2014**, *5*, 3539-3544.

[7] Chen, Q.; Luo, L. Correlation between Gas Bubble Formation and Hydrogen Evolution Reaction Kinetics at Nanoelectrodes. *Langmuir* **2018**, *34*, 4554-4559.

[8] Chen, Q.; Luo, L.; White, H. S. Electrochemical Generation of a Hydrogen Bubble at a Recessed Platinum Nanopore Electrode. *Langmuir* **2015**, *31*, 4573-4581.

[9] Edwards, M. A.; White, H. S.; Ren, H. Voltammetric Determination of the Stochastic Formation Rate and Geometry of Individual $H_2$, $N_2$, and $O_2$ Bubble Nuclei. *ACS Nano* **2019**, *13*, 6330-6340.

[10] Wang, Y.; Gordon, E.; Ren, H. Mapping the Nucleation of $H_2$ Bubbles on Polycrystalline Pt *via* Scanning Electrochemical Cell Microscopy. *J. Phys. Chem. Lett.* **2019**, *10*, 14, 3887-3892.

[11] Liu, Y.; Jin, C.; Liu, Y.; Hernandez Ruiz, K.; Fan, Y.; White, H. S.; Chen, Q. Visualization and Quantification of Electrochemical $H_2$ Bubble Nucleation at Pt, Au, and $MoS_2$ Substrates. *ACS Sens.* **2020**, DOI:101021/acssensors.0c00913.

[12] Jing, C. Gu, Z. Long, Y.-T. Imaging Electrocatalytic Processes on Single Gold Nanorods. *Faraday Discuss.* **2016**, *193*, 371-385.

[13] Wang, Y.; Shan, X.; Tao, *N.* Emerging Tools for Studying Single Entity Electrochemistry. *Faraday Discuss.* **2016**, *193*, 9-39.

[14] Zhang, L. ; Zhang, Y.; Zhang, X.; Li, Z.; Shen, G.; Ye, M.; Fan, C.; Fang, H.; Hu, J. Electrochemically Controlled Formation and Growth of Hydrogen Nanobubbles. *Langmuir* **2006**, *22*, 8109-8113.

[15] Yang, S.; Tsai, P.; Kooij, E. S.; Prosperetti, A.; Zandvliet, H. J. W.; Lohse, D. Electrochemically Generated Nanobubbles on Highly Orientated Pyrolytic Graphite Surfaces. *Langmuir* **2009**, *25*, 1466-1474.

[16] Dollekamp, E.; Bampoulis, P.; Poelsema, B.; Zandvliet, H. J. W.; Kooij, E. S. Electrochemically Induced Nanobubbles between Graphene and Mica. *Langmuir* **2016**, *32*, 6582-6590.

[17] Liu, Y.; Dillon, S. J. *In Situ* Observation of Electrolytic $H_2$ Evolution Adjacent to Gold Cathodes. *Chem. Commun.* **2014**, *50*, 1761-1763.

[18] Kim, Q.; Shin, D.; Park, J.; Weitz, D. A.; Jhe, W. Initial Growth Dynamics of 10 nm Nanobubbles in the Graphene Liquid Cell. *Appl. Nanosci.* **2018, 1-7**. DOI:10.1007/s13204-018-0925-3.

[19] Hao, R.; Fan, Y.; Anderson, T. J.; Zhang, B. Imaging Single Nanobubbles of $H_2$ and $O_2$ During the Overall Water Electrolysis with Single-Molecule Fluorescence Microscopy. *Anal. Chem.* **2020**, *92*, 3682-3688.

[20] Hao, R.; Fan, Y.; Howard, M. D.; Vaughan, J. C.; Zhang, B. Imaging Nanobubble Nucleation and Hydrogen Spillover during Electrocatalytic Water Splitting. *Proc. Natl. Acad. Sci.* **2018**, *115*, 5878-5883.

[21] Karim, W.; Spreafico, C.; Kleibert, A.; Gobrecht, J.; VandeVondele, J.; Ekinci, Y.; van Bokhoven, J. A. Catalyst Support Effects on Hydrogen Spillover. *Nature* **2017**, *541*, 68-71.

[22] Wang W. Imaging the Chemical Activity of Single Nanoparticles with Optical Microscopy. *Chem. Soc. Rev.* **2018**, *47*, 2485-2508.

[23] Jing, C.; Reichert, J. Nanoscale Electrochemistry in the "Dark-Field". *Curr. Op. Electrochem.* **2017**, *6*, 10-16.

[24] Hoener, B. S.; Kirchner, S. R.; Heiderscheit, R. S.; Collins, S. E.; Chang, W.-S.; Link, S.; Landes, C. F. Plasmonic Sensing and Control of Single Nanoparticle Electrochemistry. *Chem.* **2018**, *4*, 1560-1585.

[25] Collins, S. S. E.; Cittadini, M.; Pecharroman, C.; Martucci, A.; Mulvaney, P. Hydrogen Spillover between Single Gold Nanorods and Metal Oxide Supports: A Surface Plasmon Spectroscopy Study. *ACS Nano* **2015**, *9*, 7846-7856.

[26] Wang, Y.; Chen, J.; Jiang, Y.; Wang, X.; Wang, W. Determining the Subnanometer Thickness of the Water-Depletion Layer at the Interface between Water and the Hydrophobic Substrate. *Anal. Chem.* **2019**, *91*, 4665-4671.

[27] Chen, J.; Zhou, K.; Wang, Y.; Gao, J.; Yuan, T.; Pang, J.; Tang, S.; Chen, H.-Y.; Wang, W. Measuring the Activation Energy Barrier for the Nucleation of Single Nanosized Vapor Bubbles. *Proc. Natl. Acad. Sci.* **2019**, *116*, 12678-12683.

[28] Lemineur, J.-F.; Noël, J.-M.; Ausserré, D.; Combellas, C.; Kanoufi, F. Combining Electrodeposition and Optical Microscopy for Probing Size-Dependent Single-Nanoparticle Electrochemistry. *Angew. Chem. Int. Ed.* **2018**, *57*, 11998-12002.

[29] Lemineur, J.-F.; Noël, J.-M.; Combellas, C.; Ausserré, D.; Kanoufi, F. The Promise of Antireflective Gold Electrodes for Optically Monitoring the Electro-Deposition of Single Silver Nanoparticles. *Faraday Discuss.* **2018**, 210, 381-395.

[30] Lemineur, J.-F.; Noël, J.-M.; Combellas, C.; Kanoufi, F. Optical Monitoring of the Electrochemical Nucleation and Growth of Silver Nanoparticles on Electrodes: From Single to Ensemble Nanoparticles Inspection. *J. Electroanal. Chem.* **2020**, 114043.

[31] Mahamdeh, M.; Simmert, S.; Luchniak, A.; Schäffer, E.; Howard, J. Label-Free High-Speed Wide-Field Imaging of Single Microtubules using Interference Reflection Microscopy. *J. Microsc.* **2018**, *272*, 60-66

[32] Orbach, R.; Howard, J. The Dynamic and Structural Properties of Axonemal Tubulins Support the High Length Stability of Cilia. *Nat. Commun.* **2019**, *10*, 1838.

[33] Campidelli, S.; Khachfe, R. A.; Jaouen, K.; Monteiller, J.; Amra, C.; Zerrad, M.; Cornut, R.; Derycke, V.; Ausserré, D. Backside Absorbing Layer Microscopy: Watching Graphene Chemistry. *Sci. Adv.* **2017**, *3*, 1-6.

[34] Sevenler, D.; Avci, O.; Ünlü, M. S. Quantitative Interferometric Reflectance Imaging for the Detection and Measurement of Biological Nanoparticles. *Biomed. Opt. Express* **2017**, *8*, 2976-2989.

[35] Lemineur, J.-F.; Stockmann, T. J.; Médard, J.; Smadja, C.; Combellas, C.; Kanoufi, F. Optical Nanoimpacts of Dielectric and Metallic Nanoparticles on Gold Surface by Reflectance Microscopy: Adsorption or Bouncing? *J. Anal. Testing* **2019**, *3*, 175-188.

[36] Lemineur, J.-F.; Noël, J.-M.; Courty, A.; Ausserré, D.; Combellas, C.; Kanoufi, F. *In Situ* Optical Monitoring of the Electrochemical Conversion of Dielectric Nanoparticles: From Multistep Charge Injection to Nanoparticle Motion. *J. Am. Chem. Soc.* **2020**, *142*, 7937-7946.

[37] Hassel, A.W.; Lohrengel, M.M. The Scanning Droplet Cell and Its Application to Structured Nanometer Oxide Films on Aluminium. *Electrochim. Acta* **1997**, *42*, 3327-3333.

[38] Ebejer, N.; Güell, A. G.; Lai, S. C. S.; McKelvey, K.; Snowden, M. E.; Unwin, P.R. Scanning Electrochemical Cell Microscopy: A Versatile Technique for Nanoscale Electrochemistry and Functional Imaging. *Annu. Rev. Anal. Chem.* **2013**, *6*, 329-351.

[39] Saha, P.; Hill, J. W.; Walmsley, J. D.; Hill, C. M. Probing Electrocatalysis at Individual Au Nanorods *via* Correlated Optical and Electrochemical Measurements. *Anal. Chem.* **2018**, *90*, 12832-12839.

[40] Li, W.; Wojcik, M.; Xu, K. Optical Microscopy Unveils Rapid, Reversible Electrochemical Oxidation and Reduction of Graphene. *Nano Lett*. **2019**, *19*, 983-989.

[41] Shan, X.; Diez-Perez, I.; Wang, L.; Wiktor, P.; Gu, Y.; Zhang, L.; Wang, W.; Lu, J.; Wang, S.; Gong, Q.; Li, J.; Tao N. Imaging the Electrocatalytic Activity of Single Nanoparticles. *Nat. Nanotech.* **2012***, 7*, 668-672.

[42] Wang, Y.; Chen, J.; Jiang, Y.; Wang, X.; Wang, W. Label-Free Optical Imaging of the Dynamic Stick-Slip and Migration of Single Sub-100-nm Surface Nanobubbles: A Superlocalization Approach. *Anal. Chem.* **2019**, *91*, 4665-4671.

[43] Xu, S.; Yu, X.; Chen, Z.; Zeng, Y.; Guo, L.; Li, L.; Luo, F.; Wang, J.. Qiu, B.; Lin, Z. Real-Time Visualization of the Single-Nanoparticle Electrocatalytic Hydrogen Generation Process and Activity under Dark Field Microscopy. *Anal. Chem.* **2020**, *92*, 9016-9023.

[44] Epstein, P.S.; Plesset, M. S. On the Stability of Gas Bubbles in Liquid-Gas Solutions. *J. Chem. Phys.* **1950**, *18*, 1505-1509.

[45] Davies, T. J.; Compton, R. G. The Cyclic and Linear Sweep Voltammetry of Regular and Random Arrays of Microdisc Electrodes: Theory. *J. Electroanal. Chem.* **2005**, *585*, 63-82.

[46] Henstridge, M. C.; Compton, R. G. Mass Transport to Micro- and Nanoelectrodes and Their Arrays: A Review. *Chem. Record* **2012**, *12*, 63-71.

[47] Lohse, D.; Zhang, X. Pinning and Gas Oversaturation Imply Stable Single Surface Nanobubbles. *Phys. Rev. E* **2015**, *91*, 031003(R).

[48] Brenner, M. P.; Lohse, D. Dynamic Equilibrium Mechanism for Surface Nanobubble Stabilization. *Phys. Rev. Lett*. **2008**, *101*, 214505 and references therein.

[49] German, S. R.; Edwards, M. A.; Chen, Q.; White, H. S. Laplace Pressure of Individual $H_2$ Nanobubbles from Pressure-Addition Electrochemistry. *Nano Lett*. **2016**, *16*, 6691-6694.

[50] Wei, W; Yuan, T.; Jiang, W.; Gao, J.; Chen, H.-Y.; Wang, W. Accessing the Electrochemical Activity of Single Nanoparticles by Eliminating the Heterogeneous Electrical Contacts. *J. Am. Chem. Soc.* **2020**, *142*, 14307-14313.

[51] Ustarroz, J.; Ornelas, I. M.; Zhang, G.; Perry, D.; Kang, M.; Bentley, C. L.; Walker, M.; Unwin, P. R. Mobility and Poisoning of Mass-Selected Platinum Nanoclusters during the Oxygen Reduction Reaction. *ACS Catal.* **2018**, *8*, 6775-6790.

[52] Kong, L.; Mayorga-Martinez, C. C.; Guan, J.; Pumera, M. Photocatalytic Micromotors Activated by UV to Visible Light for Environmental Remediation, Micropumps, Reversible Assembly, Transportation, and Biomimicry. *Small* **2019**, 1903179.

[53] Gibbs, J. G.; Zhao, Y.-P. Autonomously Motile Catalytic Nanomotors by Bubble Propulsion. *Appl. Phys. Lett.* **2009**, *94*, 163104.

[54] Gao, W.; Feng, X.; Pei, A.; Gu, Y.; Li, J.; Wang, J. Seawater-Driven Magnesium Based Janus Micromotors for Environmental Remediation. *Nanoscale* **2013**, *5*, 4696-4700.

[55] Chen, X.; Maljusch, A.; Rincón, R. A. ; Battistel, A.; Bandarenka, A. S.; Schuhmann, W. Local Visualization of Catalytic Activity at Gas Evolving Electrodes Using Frequency-Dependent Scanning Electrochemical Microscopy. *Chem. Commun.* **2014**, *50*, 13250-13253.

[56] Zeradjanin, A. R.; Ventosa, E; Bondarenko, A. S. Schuhmann, W. Evaluation of the Catalytic Performance of Gas-Evolving Electrodes Using Local Electrochemical Noise Measurements. *ChemSusChem* **2012**, *5*, 1905 – 1911.

[57] Bentley, C. L.; Edmondson, J.; Meloni, G. N.; Perry, D.; Shkirskiy, V.; Unwin, P. R. Nanoscale Electrochemical Mapping. *Anal. Chem.* **2019**, *91*, 84-108.

[58] Bentley, C. L.; Kang, M.; Unwin, P. R. Nanoscale Surface Structure–Activity in Electrochemistry and Electrocatalysis *J. Am. Chem. Soc.* **2019**, *141*, 6, 2179–2193.

Insert Table of Contents artwork here